Check for updates

Nanomechanical elasticity and fracture studies of lithium phosphate (LPO) and lithium tantalate (LTO) solid-state electrolytes†

Maedeh Amirmaleki, [ID] [a] Changhong Cao, [ID] [a] Biqiong Wang,[b] Yang Zhao, [ID] [b] Teng Cui, [ID] [a] Jason Tam, [ID] [c] Xueliang Sun, [ID] *[b] Yu Sun[a] and Tobin Filleter [ID] *[a]

All-solid-state batteries (ASSBs) have attracted much attention due to their enhanced energy density and safety as compared to traditional liquid-based batteries. However, cyclic performance depreciates due to microcrack formation and propagation at the interface of the solid-state electrolytes (SSEs) and electrodes. Herein, we studied the elastic and fracture behavior of atomic layer deposition (ALD) synthesized glassy lithium phosphate (LPO) and lithium tantalate (LTO) thin films as promising candidates for SSEs. The mechanical behavior of ALD prepared SSE thin films with a thickness range of 5 nm to 30 nm over suspended single-layer graphene was studied using an atomic force microscope (AFM) film deflection technique. Scanning transmission electron microscopy (STEM) coupled with AFM was used for microstructural analysis. LTO films exhibited higher stiffness and higher fracture forces as compared to LPO films. Fracture in LTO films occurred directly under the indenter in a brittle fashion, while LPO films failed by a more complex fracture mechanism including significant plastic deformation prior to the onset of complete fracture. The results and methodology described in this work open a new window to identify the potential influence of SSEs mechanical performance on their operation in flexible ASSBs.

Introduction

Interest in Li-ion batteries (LIBs) is constantly growing from portable electronics; to electric vehicles; to flexible batteries in wearable electronics.[1–3] Along with this increasing demand for LIBs, substitution of conventional flammable and volatile liquid electrolytes with inorganic solid-state electrolytes (SSEs) is essential to improve the safety and capabilities of the batteries.[4] Thin film based all-solid-state batteries (ASSBs) facilitate miniaturization of microelectronic devices and flexible batteries with higher safety and energy densities.[2] In addition to the chemical and electrochemical stability, mechanical stability in particular at the interface of SSE/electrode of ASSBs is also essential for the batteries performances. On one hand, microcracks can form due to elevated internal and/or external stresses, leading to the crack propagation, delamination, and

fragmentation of electrodes and SSEs/electrode interfaces. For example, electrode volume changes during charging/discharging increases internal stresses and introduces bending/stretching to the SSE which eventually aggregate the formation of microcracks.[5–9] On the other hand, Li dendrite formation and growth introduces stress at the SSE/Li electrode interface that results in mechanical deformation which is the very complex phenomena because all chemical, electrochemical, and mechanical factors are involved.[6,10] Two main types of SSEs are polymer and inorganic electrolytes. Polymer SSEs are believed to facilitate the interfacial contact issues due to their soft and flexible nature, however the volume changes of electrodes especially Li anode, introduce partial delamination at the interface.[11] Inorganic ceramic SSEs are also fabricated because of their higher strength and stability in air, while their poor interface stability remains as an issue.[12] Among thin film fabrication techniques, atomic layer deposition (ALD) enables uniform, pinhole-free ultra-thin films which provides good interfacial contact between inorganic SSEs/electrodes.[13–15] Despite such contact establishment, the contact needs to be mechanically stable. Previous research has suggested that elastic deformation of SSEs materials accompanied by some degree of ductility is desirable to maintain good interfacial contact with an electrode during cycling in order to preserve the battery cycling performance.[13,14,16] Low stiffness sulfide SSEs with a low range of Young's

[a]*Department of Mechanical and Industrial Engineering, University of Toronto, 5 King's College Rd, Toronto, ON, Canada, M5S 3G8. E-mail: filleter@mie.utoronot.ca*
[b]*Department of Mechanical and Materials Engineering, University of Western Ontario, London, Ontario, Canada N6A 5B9. E-mail: xsun9@uwo.ca*
[c]*Department of Materials Science and Engineering, University of Toronto, 184 College St, Toronto, ON, Canada, M5S 3E4*
†Electronic supplementary information (ESI) available. See DOI: 10.1039/c9nr02176k

modulus (E) (14–25 GPa for Li_2S-P_2S_5)[8,17,18] were considered as favorable SSEs for the bulk battery design to accommodate volume changes of the electrodes.[8] However, Bucci et al.[19] developed a cohesive zone model to simulate damage evaluation and presented quantitative conditions that facture would occur. They indicated that electrolytes with $E \sim 15$ GPa were more prone to micro-cracking in compare to SSEs with higher E. Based on this model for SSEs with $E = 15$ GPa, fracture was prevented when the electrode expansion was below 7.5%, and the fracture energy of SSEs was greater than $G_c = 4$ J m^{-2}. In addition, oxide electrolytes exhibiting high E (77, 150, and 192 GPa in amorphous LLZO, LIPON, and $Li_{0.33}La_{0.57}TiO_3$, respectively)[16,20,21] have been reported; however, the impact of inorganic SSEs mechanical behavior on battery performance is unknown. Moreover, there are a few models that incorporated electro-chemo-mechanical behavior of solid electrolytes to address interface stability in contact with Li metal. Li nucleation in the grain boundary of ceramic electrolyte was modeled by Raj and Wolfenstine[22] with coupling mechanical stresses and the electrical potential. They showed that critical current above Li nucleation depends on ionic conductivity and fracture strength of the SSE. Monroe and Newman[23,24] modeled the lithium deposition in a polymer electrolyte and considered the contribution of bulk and surface stresses to Li deposition electrochemical reactions. They concluded that deposition stability increased by increasing electrolyte shear modulus because of more contribution of bulk pressure and surface stresses. Based on Monroe and Newman model,[24] researchers constructed hybrid SSEs with high modulus (elastic of shear modulus) to suppress dendrite formation and growth, however it has been found that Li dendrite can grow and penetrate both polymer and rigid ceramics.[25–27] It is still unclear which model can explain the mechanisms of Li dendrite growth. The SSE modulus is not the only mechanical factor that limits the Li dendrite growth and other mechanical properties such as tensile strength, fracture toughness, and flexure strength of brittle inorganic SSEs require more attention. Recently

organic, inorganic and hybrid coating layers have shown potentials for suppressing Li dendrite at the interface of SSE/Li metal.[15] Fu et al.,[28] designed and developed a hybrid system of polymer embedded with nano-sized ceramic domains called as "soft ceramic" structure as dendrite-suppressing SSE by applying a universal chemomechanical model that can assess fundamentally pressure- or density-driven dendrite suppressing. In addition to all the efforts on modelling and designing compatible interfaces, a study by LePage et al.[29] showed that "creep" is a dominant deformation mechanism for Li metal in batteries which further complicates the interfacial mechanical stability issues. These studies show that better understanding of mechanical behavior of nanoscale organic and inorganic SSEs are essential prior to investigate their theoretical and experimental electro-chemomechanical implications.

Previously studied amorphous LPO and LTO thin films with moderate ionic conductivity ($\sim 10^{-8}$ S cm^{-1} at 25 °C) have been used as SSEs for ASSBs,[30,31] and as coating layers on the electrodes of LIBs to significantly improve the battery performance.[31–35] A summary of electrochemical studies of the impact of LTO and LPO coatings on electrode materials in LIBs cyclic performance is presented in Table 1. Both LPO and LTO exhibited electrochemical and chemical stability, and ionic conductivity for coating cathode materials as well as facilitating better contact between electrode materials and electrolytes as shown in Table 1.[31–34] The mechanism behind preserving the structural degradation of electrode material is not well understood and a more detailed understanding of the mechanical stability of SSEs in ASSBs against internal and/or external stresses during charging/discharging is needed.[14,15] In this study, the elastic and fracture behavior of ALD prepared LTO, and LPO SSEs thin films were studied and compared for the first time. The mechanical behavior of a range of ultra-thin ALD prepared suspended SSEs thin films (5 nm–30 nm thickness) were studied using an atomic force microscope (AFM) film deflection technique. The film under AFM deflection emulates

Table 1 Summary of electrochemical impact of LTO and LPO thin film on ASSBs as coating materials

Coating type	Fabrication method	Film thickness	Coating electrode type	Electrochemical cycling condition	Introduced benefits to ASSB by coating
LiTaO$_3$	ALD[31]	5–10 nm	$LiNi_{1/3}Co_{1/3}Mn_{1/3}O_2$ (NMC) cathode	Capacity of 155 mA h g^{-1} and 145 mA h g^{-1} upon 100 cycles within 3.0–4.6 V and 3.0–4.7 V, respectively	5 cycles ALD LTO is effective towards improving cyclic performance of the NMC cathode with upper cut-off potential <4.8 V. 10 cycles ALD LTO is the best effect in decreasing NMC electrode degradation with a cut-off potential of 3.0–4.8V
	Spin coating[34]	~150 nm	Interfaces between LiCoO$_2$ cathode and sulfide SSE	—	Reduced the interfacial resistance and improved high-rate capability
LiPO$_3$	ALD[32] (nano composite of TiO$_2$/LPO)	~23 nm	CNT anodes	Capacity of 204 mA h g^{-1} upon 200 cycles within 1.0–3.0 V	Improve capacity and rate capability of CNT anodes at high current rates
	ALD[33]	~10 nm	$LiNi_{0.76}Mn_{0.14}Co_{0.10}O_2$ (nickel-rich NMC) cathode	Capacity of 190 mA h g^{-1} upon 200 cycles within 2.7–4.5 V at C/3	Dramatically enhanced cycling stability of the cathode by improving interfacial kinetics. Eliminated cracking of cathode particle by infusing into the grain boundary

stress levels present in the SSE at the nanoscale, and the results will help to identify the potential influence of SSEs mechanical performances for on their operation in flexible ASSBs.

Materials

Monolayer chemical vapor deposition (CVD) grown graphene on a holey Si_3N_4 TEM grid with a hole diameter of 2.5 μm was used as a supporting layer for ALD SSEs thin films as illustrated in Fig. 1a. In addition, a thin layer of 20 cycles ALD Al_2O_3 (~2 nm thick) was deposited on top of the SSEs films to avoid oxide layer formation upon air exposure.[30,31,36] An ALD technique was used to deposit amorphous LTO, LPO and Al_2O_3 thin films at 235 °C, 275 °C and 120 °C, respectively. The thicknesses of the films were controlled by varying ALD cycles. 10, 30, and 50 cycles of ALD LTO films with a deposition rate of 5 Å per cycle were deposited over graphene.[31] 100, 300, and 500 cycles of LPO ALD films with a deposition rate of 0.6 Å per cycle were deposited over graphene.[30] It was previously reported that the film thickness of LTO and LPO is linearly dependent on ALD cycle number when deposited on Si substrates due to the self-limiting nature of the ALD process.[30,31] The ALD growth rate of the films was assumed to be similar to that on a Si substrate in this work and the thicknesses were calculated to be 5 nm, 15 nm and 25 nm for LTO, and 6 nm, 18 nm, and 30 nm for LPO films.[30,31] As it is shown schematically in Fig. 1a, a sandwich structure of LTO/Al_2O_3 and LPO/Al_2O_3 was formed on both side of the single layer graphene due to the conformal design of the ALD method, and for brevity, this multilayer structure is referred to as "SSEs film". In this structure, the Al_2O_3 is used to protect the SSE layer from air exposure similar to Al_2O_3 coatings that are used in real ASSB configurations to protect SSEs from chemical reactions with Li metal. Al_2O_3 coating layers help to reduce the interfacial resistance in the interface of SSE and Li anodes as well as blocking side reactions between cathode and SEEs at their interfaces.[37,38]

Results and discussion

Microstructural analysis of the SSEs films was performed using STEM to evaluate the SSEs film coverage and determine the crystallinity of the structures. Fig. 1b–e, show annular-dark-field (ADF) images, secondary electron microscopy (SEM) images, and selected area diffraction patterns (SADP) of the LTO (15 nm and 25 nm) and LPO (18 nm and 30 nm) films. No cracks or observable major defects were observed on the sample surface. The white arrows in Fig. 1b reveal discontinuity on the surface of the film prepared with 30 ALD cycles LTO (15 nm), while the film prepared with 300 ALD cycles LPO (see Fig. 1d) with similar film thickness (18 nm) showed a continuous full coverage over graphene. This is likely due to the higher number of the LPO ALD cycles (or smaller rate of deposition) that provided a long time to form a continuous film. It is also shown that thicker LTO films (Fig. 1c) prepared with 50 cycles ALD (25 nm) were continuously formed. SADP of LTO films (Fig. 1b and c) revealed that all of the layers were amorphous while the single layer graphene diffraction pattern was presented and marked with red circles (see clearly in ESI Fig. S1†). SADP of the LPO samples (Fig. 1d and e) also showed an amorphous halo pattern; however, nanocrystalline spots were also visible suggesting that LPO samples were not entirely amorphous. Circular particles were also observed on the surfaces of the both SSEs films (shown with red arrows in Fig. 1b–e) containing the same elements as the SSEs films as confirmed using energy-dispersive X-ray spectroscopy (EDS) mapping (see ESI Fig. S2†).

The elastic behavior of LTO (5 nm, 15 nm, and 25 nm) and LPO (6 nm, 18 nm, and 30 nm) thin films prepared by ALD was investigated and compared by conducting AFM film deflection. Tapping mode AFM topography imaging was performed prior to elastic deflection to align the AFM diamond tip in the middle of the holes, and to identify defective and damage free films prior to deflection. After elastic deflection, tapping mode imaging was also performed again to ensure that no damage occurred. For each film thickness, at least seven independent freestanding films were measured. As shown schematically in Fig. 2a, the AFM tip was deflected in the middle of the freestanding films with a maximum normal force of 100 nN at a constant displacement rate of 10 μm s^{-1}. Details of data processing is presented in Fig. S3 of ESI.† No
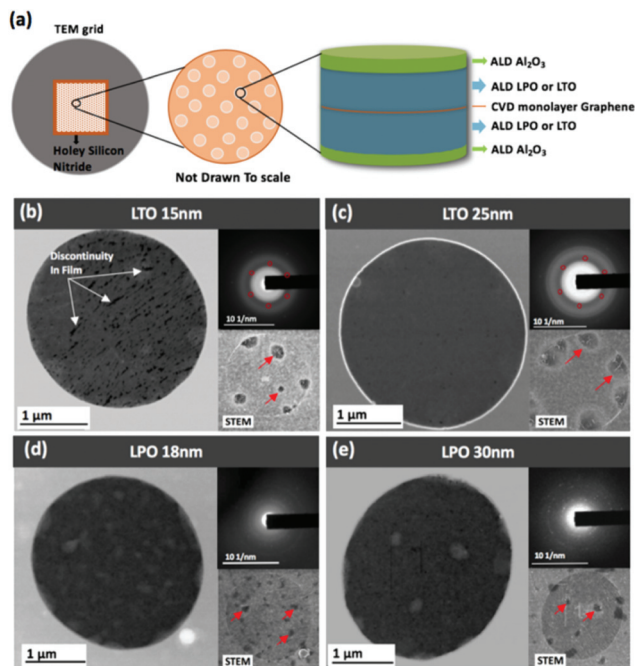

Fig. 1 (a) Schematic of holey silicon nitride (hole diameter of 2.5 μm) TEM grid with multilayer thin films of LTO or LPO. Microstructural analysis using STEM imaging including ADF, SEM, and SADP images of (b) LTO 15 nm, (c) LTO 25 nm, (d) LPO 18 nm, and (e) LPO 30 nm thin films (thicknesses are referring to LTO of LPO layer only). Red circles show diffraction pattern of monolayer graphene and red arrows refer to circular shaped particles over the film surfaces.
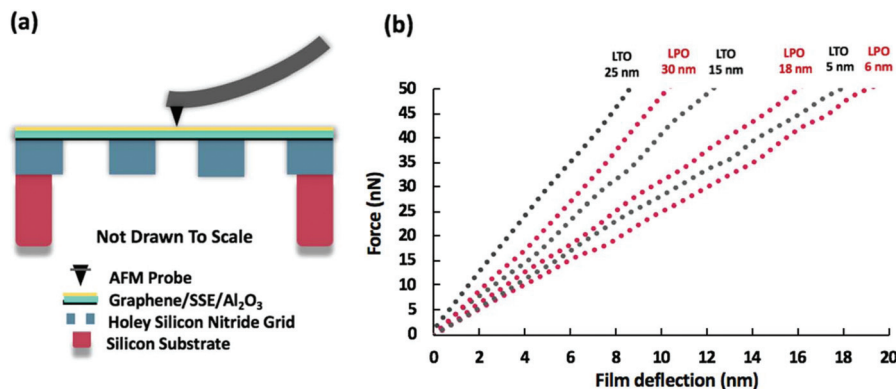
Fig. 2 (a) Schematic cross section view of elastic AFM deflection experiments on LPO and LTO films suspended over holey silicon nitride TEM grids. (b) Representative loading force–film deflection curves of LPO and LTO thin films with different ALD cycles (thickness of the LPO and LTO layer shown). All thin films were deposited on single-layer graphene and capped with 20 cycles ALD Al_2O_3.

significant hysteresis was observed between loading–unloading curves (see ESI Fig. S4†). This indicates that bonding between layers in thin structured films, and between the graphene/substrate was strong enough to avoid any significant slippage between layers. Fig. 2b shows representative normal force–film deflection curves recorded for both SSEs materials with different thicknesses (LTO: 5 nm, 15 nm, 25 nm, and LPO: 6 nm, 18 nm, 30 nm). The results of all samples were consistent and repeatable (an example is shown in ESI Fig. S5†). As expected by increasing the film thickness, higher forces were required to indent thin films to equivalent film deflections for both SSEs films, indicating an increase in mechanical stiffness of the films. Furthermore, LTO films were found to exhibit higher stiffness (for comparable thicknesses) than LPO films at all thicknesses. On the other word, LPO films show more flexibility whereas here flexibility is defined as the inverse of stiffness. It should be noted that models typically used to calculate the elastic modulus of suspended circular sheets under a central point load are limited to thin films that are made of isotropic elastic materials such as graphene, MoS_2, WS_2, and WSe_2 and less complex multilayer structures (refer to ESI section 6† for details of the model application).[39–43] The application of those models is limited for the LTO and LPO films in this study, as they were supported by single-layer graphene and capped with ~2 nm layer of Al_2O_3, and therefore quantifying the elastic modulus of the SE films was not conducted. The models can however, provide insight into the mechanical effects of the support and capping layers (ESI section 6†).

In addition to elastic behavior studies, we investigated the failure behavior of the SSEs thin films. The center of the films were mechanically loaded until fracture by AFM deflection testing. The term "failure" is used to indicate the significant fracture of the films and was identified by an abrupt force drop to or beyond 20% of the maximum force.[44] Fracture following this maximum force was confirmed by tapping mode AFM topography imaging after film deflection to failure (as shown in Fig. 3a). At least seven independent freestanding films were tested to failure for each thickness. The failure

loads were found to be larger for increasing the film thickness for both SSEs thin films as expected (see Fig. 3b). All LTO films failed at greater loads than LPO films.

Although, the thickness range of the LTO and LPO films was similar, normalizing the maximum load by the total thickness (i.e., F/t) was performed to normalize thickness effects on the failure forces to facilitate a more direct comparison between the films intrinsic behavior. Fig. 3c reveals an observed thickness-dependency of the normalized failure forces of both SSEs films at all thicknesses as normalized failure forces were observed to decrease for thicker films. Moreover, the normalized failure force decay was more significant when the thickness increased from 5 nm to 15 nm for LTO and 6 nm to 18 nm for LPO films. The higher normalized failure forces of LTO 5 nm and LPO 6 nm as compared to the thicker cases was attributed to the influence of the higher Young's modulus values of the Al_2O_3 (with $E = 168–182$ GPa)[45] capping layer and single-layer graphene (with $E = 1.0 \pm 0.1$ TPa)[41] support layer. This influence becomes greater when the thickness ratio of "SSEs film to Al_2O_3 layer" and/or that of "SSEs film to graphene layer" are reduced. To further investigate the influence of Al_2O_3 and single-layer graphene on the very thin SSEs films, the normalized failure forces of LTO 5 nm and LPO 6 nm films were compared with 2 and 5 nm ALD prepared Al_2O_3 film over single-layer graphene, as shown in Fig. 3d. For 2 nm Al_2O_3 thin films, the normalized failure force was more than double that of the 5 nm Al_2O_3 thin films. The thickness dependency in the mechanical behavior of Al_2O_3 thin films was also reported by Jen et al.[46] where the critical compressive and tensile strain was found to increase by reducing the Al_2O_3 film thickness on polymer substrates. In addition, our previous study revealed the role of single-layer graphene in enhancing the mechanical performance of very thin oxide films, which can further emphasize the influence of the Al_2O_3 capping and graphene support layer on failure forces of thinner SSE films.[47]

STEM imaging was performed to study the fracture surfaces of SSEs films. As shown in Fig. 4, all of the SSEs thin films
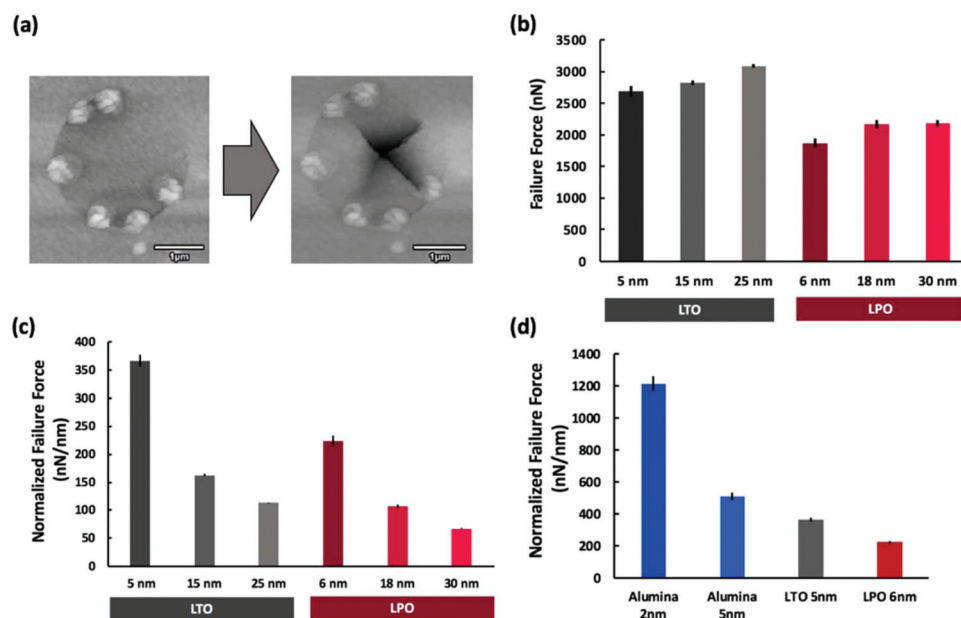
Fig. 3 (a) AFM topography image of LTO film before and after failure, (b) comparison between failure forces of LTO and LPO thin films at all thicknesses, (c) comparison between normalized failure force with respect to the total film thickness of LTO and LPO thin film at all thicknesses, and (d) comparison between normalized failure force to total film thickness of very thin LTO and LPO to 2 nm and 5 nm Al$_2$O$_3$/graphene thin films.
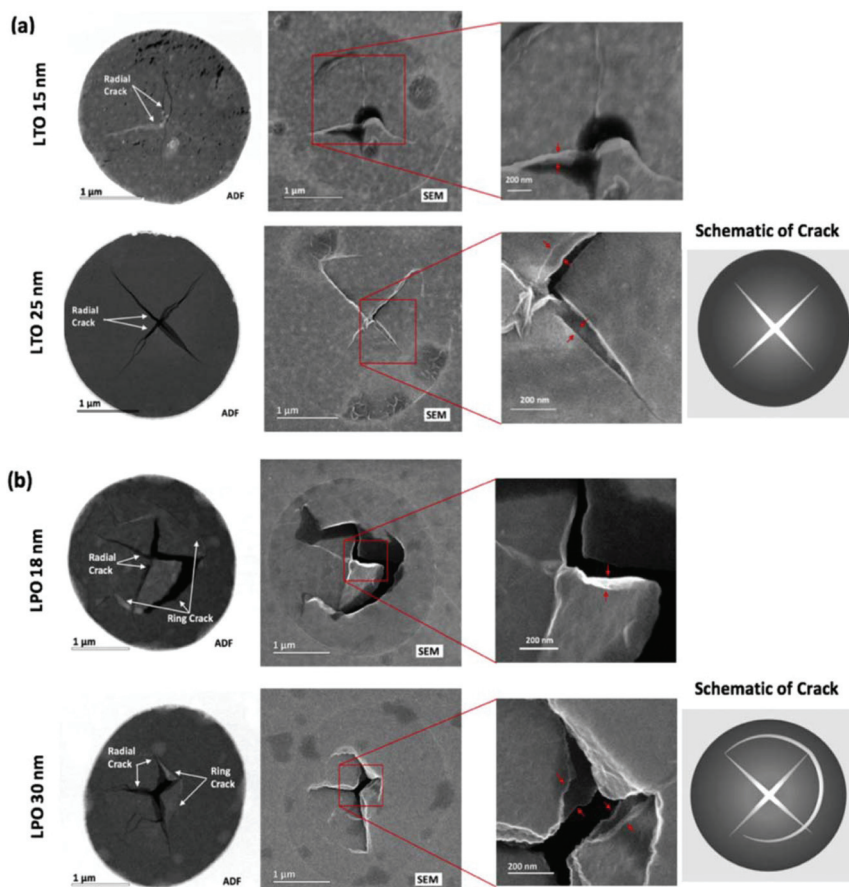

Fig. 4 Comparison of ADF and SEM images of the failed SSE films (a) LTO films of 15 nm and 25 nm, and schematic of crack, and (b) LPO films of 18 nm and 30 nm, and schematic of crack. White arrows indicate the type of cracks and red arrows indicate delamination in the films.

failed by crack initiation and propagation in the middle of films under the diamond tip. Similar to nanoindentation of thin films,[48] in AFM deflection a crack occurred under the tip of indenter (contact edge) due to stress concentration. A crack initiated under the tip and propagated along the contact edge is mainly a radial crack. LTO thin films (Fig. 4a and schematic of crack) primarily failed with radial crack formation and propagation while LPO thin films (see Fig. 4b and schematic of crack) primarily failed by both radial and semi-ring like cracks. The radial cracks occurred at the contact edge of the AFM tip (90° cracks from pyramid trace of the diamond tip) due to load concentration and crack propagated along the edges while the semi-ring like cracks were formed away from the contact edges.

The load concentration and film stretching at the contact will introduce high tensile stresses to film layers which led to high interlayer forces and caused delamination and buckling of the film under the retracted tip as shown with red arrows in Fig. 4a and b. Delamination in the center of the films was observed in both LTO and LPO films; however, the delamination was more severe in LPO 30 nm thin films. TEM imaging did not show any evidence of delamination in the interface of Al_2O_3 and LPO or LTO films (see Fig. S6 of ESI†) and accordingly bonding between the layers is considered as nearly perfect bonding. Additionally, LPO 18 nm thin films were partially ruptured and detached from the rest of the film. STEM observations revealed that fracture occurrences were more dramatic and complex in LPO films as compared with LTO films and the reasons behind this phenomenon were investigated in detail.

Two types of semi-ring like cracks were observed in the more than 70% of the of tested LPO samples as shown schematically in Fig. 5a. The first type (in Fig. 5a, top) of semi-ring crack was close to the loaded center, which was formed along the radial crack and deviated from the radial crack propagation direction. The second type (in Fig. 5a, bottom) was a larger ring formed away from the loaded center formed independently from radial cracks. The formation of the first type of ring-like cracks may be attributed to high adhesion forces between the tip and SSEs films. To further investigate, the adhesion force was measured as the difference between the "zero baseline away from contact", and the "jump out of contact force" in the AFM force–film deflection curves. The SSE films were deflected to a force equivalent to 70%, and 80% of the average failure forces and the adhesion forces were measured.

As shown in Fig. 5b, adhesion forces of the LPO films were approximately double the adhesion forces of LTO films. As the top capping layers for both films are Al_2O_3, this higher adhesion is not attributed to a difference in the intrinsic work of adhesion between the tip and films but instead a geometrical contact area effect. Higher adhesion forces indicate that LPO films would locally wrap the apex of the sharp tip to a greater extent than LTO films which can cause buckling in the films and lead to severe small ring-like cracks and also delamination of the film during the tip retraction stage. The second type of the ring-like crack can initiate due to high bending forces before failure when the film is deflected to higher depth. The deflection depth of LTO and LPO films were compared in Fig. 5c revealing that the deflection depth of LPO films at all thickness was greater than LTO films while the failure forces and stiffness of LPO film were lower. Therefore, LPO films were exposed to greater bending forces as compared to LTO films which can explain initiating ring-like crack as a consequence of film buckling around the deflected area but far from the tip.

Aside from the measured adhesion and failure forces, an interesting behavior was also observed in the shape of force–film deflection curves of LPO films when the films were indented at very high forces. While indenting LPO 18 nm films
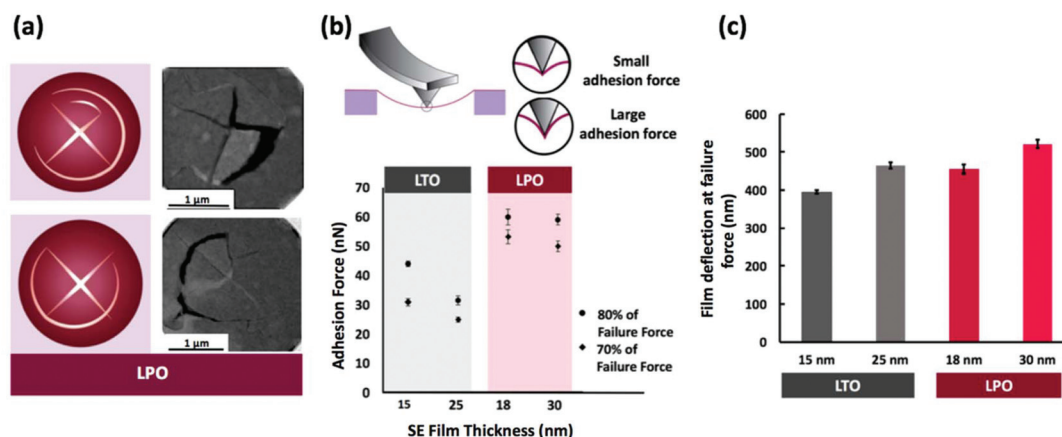

Fig. 5 (a) Schematic and STEM ADF image of types of ring-like cracks in LPO films, top: small and large semi-ring cracks close to the center of the film that deviates the radial crack direction, and bottom: larger ring away from the indenter and independent of radial cracks, (b) top: schematic of film behavior under low and high adhesion forces to the tip during tip retraction stage, bottom: adhesion forces between tip and film calculated from force–film deflection curves of SSEs films indented to the equivalent of 70%, and 80% of failure forces, (c) comparison of the deflection depth of the SSEs films at failure forces.
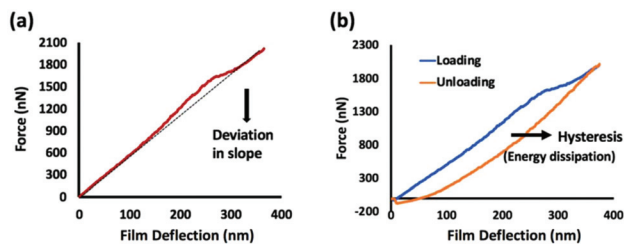
Fig. 6 Force–film deflection curve of a LPO 18 nm film loaded to 2000 nN force showing (a) slope deviation in loading curve and (b) huge hysteresis in loading–unloading curve.

to high loads, a slope deviation in the force–film deflection curve before failure was observed as shown in Fig. 6a. The slope deviation was accompanied by hysteresis in the loading/unloading curves (see Fig. 6b). The hysteresis in the loading/unloading curve indicates energy dissipation prior to the onset of failure. It should be noted that slope deviation was also observed for some LTO films, albeit to a far less extent. Fig. S7 in ESI† shows examples of the repeatability of slope deviation and hysteresis in force–film deflection curves for LPO 30 nm films. Similar slope deviation in the force–indentation curve was reported for nanoindentation of thin films over soft substrates,[48–50] and AFM deflection of multilayer graphene films.[51] In the case of thin films this was attributed to a separation of the film under the indenter *via* through thickness strains and ring-like cracks.[48–50] In case of multilayer graphene, when film deflection increased, the slippage between the middle layer and bottom layer initiated near the boundary of the suspended film and propagated along the periphery due to the localized interlayer shear at the edges and therefore

deviation and hysteresis in the force–film deflection curve was observed.[51] Analogous to these previously reported materials, when the LPO films undergo large deflection, the interlayer strains increase and the deviation in the force–film deflection curve and hysteresis in loading/unloading occur to release the interlayer strains. Therefore, the formation of large ring-like cracks away from the center of LPO films was also believed to be a consequence of releasing interlayer strains.

Differences between LTO and LPO films were also observed in the magnitude of force drops at fracture. The failure force was defined by a sudden drop in the force value during deflection. As shown in Fig. 7a, a sudden drop of failure force in LTO films (marked in green circle) was found. This large sudden drop at the failure force indicated strong bonding between the films as the LTO film failed with only radial cracks. However, for LPO films failure forces reduced more gradually (see green circles in Fig. 7b) and endured the force long after the initial failure point. The magnitude of force drop of LTO films was more than double that for LPO films, as shown in Fig. 7c. The hysteresis in the loading/unloading curves and ring-like cracks in the fractured LPO films is consistent with weak bonding between the layers in the LPO films that accommodated stress release by propagating different types of cracks and gradual failure of the film under high range loading forces.

Summary and conclusions

Herein a mechanical behavior study of ALD prepared LTO and LPO films by an AFM deflection technique was presented which enabled a comparison of the elastic and failure behavior of two promising candidates for SSEs materials in ASSBs.
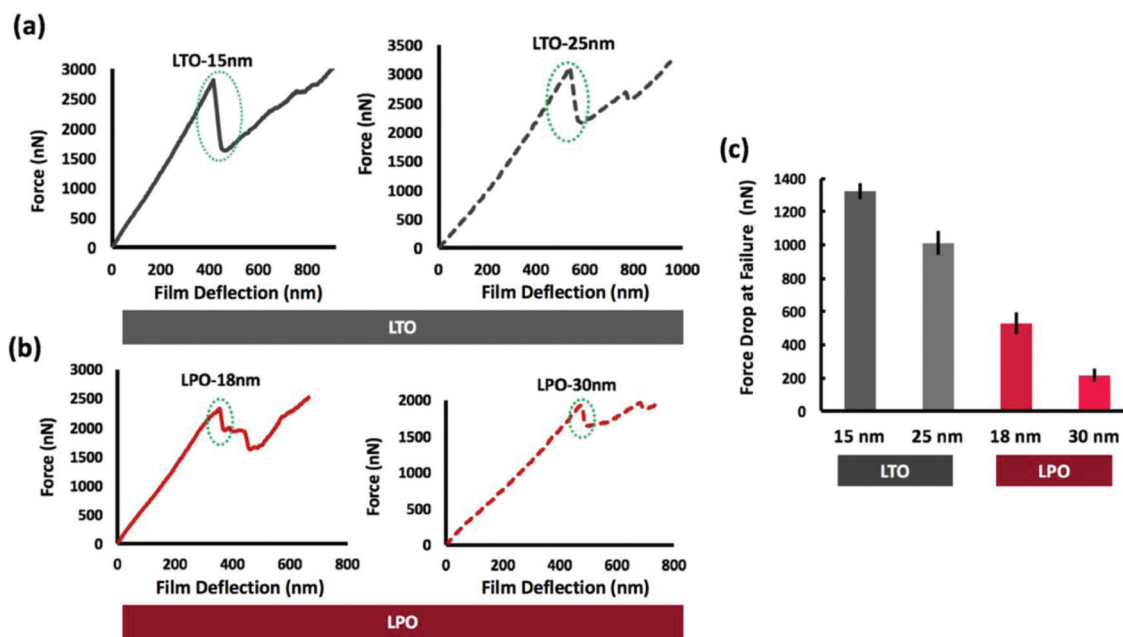

Fig. 7 Force–film deflection curves to failure, highlighting the force drop in (a) 15 nm LTO (right) and 25 nm LTO (left) thin films, and (b) 18 nm LPO (right), 30 nm LPO (left) thin films, and (c) force drop at failure *vs.* thickness of SSEs thin films.

Elastic behavior studies revealed higher stiffness or less flexibility of the LTO films as compared to LPO films. Measurements of the maximum forces that are required to fail the SSEs were also higher for LTO films as compared with LPO films. However, failure forces of very thin SSEs thin films were influenced by the capping alumina layer and graphene supporting layer to a greater extent as compared to thicker cases due to the high stiffness of the graphene and alumina layer. The results from a normalized failure force analysis indicated that the mechanical behavior of thicker films were more representative of the intrinsic behavior of the SSEs films.

Fracture surface studies revealed that LTO films failed in a more brittle manner by radial crack formation; however, LPO film exhibited both radial and semi-ring like cracks. Although delamination was present for both failed LPO and LTO films, LPO films failed in a more complex fashion with multiple types of cracking. The multiple crack mechanism and severe delamination in LPO films were partially attributed to higher adhesion forces and greater deflection depth along with interlayer shear in the LPO films. Moreover, slope deviation and energy dissipation (hysteresis) in force–displacement curve of LPO films at high forces were indicated notable plastic deformation prior to onset of complete fracture.

Nanoscale ALD prepared LTO and LPO films can be used in 2D or 3D configurations of solid-state micro batteries as SSE or coating layers for electrode materials due to their electrochemical and mechanical stabilities. The presented mechanical behavior comparison of LTO and LPO films demonstrates that LTO films exhibit higher stiffness and require higher failure forces as compared to LPO films at similar thicknesses, while LPO films have higher flexibility. Further studies are needed to determine the effect of SSE fracture strength, stiffness, and flexibility properties on crack formation and propagation under electrochemical conditions as well as electro-chemo-mechanical modeling to fully unveil phenomena behind crack formation and propagation within ASSBs. Moreover, the effect of using graphene and alumina as supporting layers to enhance the mechanical properties of very thin SSEs films was demonstrated. The results of this study opened a new window to the complex mechanical performance of the ALD SSEs materials at the nanoscale.

Methods

Suspended monolayer CVD grown graphene on holey silicon nitride TEM grid with the hole diameter of 2.5 μm (Ted Pella Inc.) was used as support for the SSEs films. LTO, LPO, and Al_2O_3 thin films were deposited at 235 °C, 275 °C and 120 °C in a Savannah 100 ALD system (Cambridge Nanotech Inc.), respectively. For LTO, ALD sub-cycles of Li_2O and Ta_2O_5 were combined. The precursors were lithium *tert*-butoxide (LiO^{t}Bu, $(CH_3)_3COLi$) for Li, tantalum(v) ethoxide (Ta(OEt)$_5$, Ta $(OC_2H_5)_5$) for Ta and H_2O with the sources temperatures of 170 °C, 170 °C and room-temperature, respectively. During the ALD process, the pulse time of LiO*t*Bu and Ta(OEt)$_5$ was 1 and

0.5 s, respectively, while H_2O was pulsed for 1 s. One ALD LTO cycle was expressed as $1 \times Li_2O + 6 \times Ta_2O_5$ cycles.

For LPO ALD deposition, the precursors were lithium *tert*-butoxide (LiO^{t}Bu, $(CH_3)_3COLi$) for lithium, trimethylphosphate [TMPO, $(MeO)_3PO$] for phosphate with the sources temperatures of 170 °C and 70 °C, respectively. During the ALD process, the pulse time of LiOTBu and TMPO was 1.5 and 1.5 s, respectively. For Al_2O_3 ALD deposition, the precursors were trimethylaluminium (TMA) for Al and H_2O under room temperature, respectively. During the ALD process, the pulse time of TMA and H_2O was 1.0 and 1.0 s, respectively. For all LTO and LPO and Al_2O_3 ALD process, precursor pulses were separated by a 20 s nitrogen gas purge. Nitrogen gas was also used as the carrier gas for all precursors with a flow rate of 20 sccm.

AFM deflection tests were conducted using an Asylum MFP-3D AFM. The cantilever (ND-DYI series, All-Diamond Probe, Nano Science Instrument) was calibrated using Sader's method[52] yielding a normal spring constant of 39 N m^{-1}. The AFM was stabilized for at least 12 h prior to experiments. The radius of the diamond AFM tip was measured using SEM Hitachi SU3500 to be ~100 nm before and after deflection tests (ESI Fig. S8a and S8b†). Hitachi HF-3300 STEM equipped with ADF and secondary electron detector was used to perform imagining and EDS elemental mapping with a beam voltage of 300 keV.

Conflicts of interest

There are no conflicts of interest to declare.

Acknowledgements

References

1 M. Armand and J. M. Tarascon, *Nature*, 2008, **451**, 652–657.
2 Y. Hu and X. Sun, *J. Mater. Chem. A*, 2014, **2**, 10712.
3 X. Wang, X. Lu, B. Liu, D. Chen, Y. Tong and G. Shen, *Adv. Mater.*, 2014, **26**, 4763–4782.
4 E. P. Roth and C. J. Orendorff, *Interface*, 2012, **21**, 45–50.
5 Y. Suzuki, K. Kami, K. Watanabe, A. Watanabe, N. Saito, T. Ohnishi, K. Takada, R. Sudo and N. Imanishi, *Solid State Ionics*, 2015, **278**, 172–176.
6 K. Kerman, A. Luntz, V. Viswanathan, Y.-M. Chiang and Z. Chen, *J. Electrochem. Soc.*, 2017, **164**, A1731–A1744.

7   J. Liu, H. Zhu and M. H. A. Shiraz, *Front. Energy Res.*, 2018, **6**, 1–5.

8   A. Sakuda, A. Hayashi and M. Tatsumisago, *Sci. Rep.*, 2013, **3**, 2261.

9   W. Zhang, D. Schröder, T. Arlt, I. Manke, R. Koerver, R. Pinedo, D. A. Weber, J. Sann, W. G. Zeier and J. Janek, *J. Mater. Chem. A*, 2017, **5**, 9929–9936.

10 P. Wang, W. Qu, W. L. Song, H. Chen, R. Chen and D. Fang, *Adv. Funct. Mater.*, 2019, **1900950**, 1–29.

11 D. Devauxa, K. J. Harryb, D. Y. Parkinsond, R. Yuana, D. T. Hallinane, A. A. MacDowelld and N. P. Balsara, *J. Electrochem. Soc.*, 2015, **162**, A1301–A1309.

12 A. Manthiram, X. Yu and S. Wang, *Nat. Rev. Mater.*, 2017, **2**, 16103.

13 C. Bae, H. Shin and K. Nielsch, *MRS Bull.*, 2011, **36**, 887–897.

14 B. V. Lotsch and J. Maier, *J. Electroceram.*, 2017, **38**, 1–14.

15 Y. Zhao, K. Zheng and X. Sun, *Joule*, 2018, **2**, 2583–2604.

16 S. Yu, R. D. Schmidt, R. Garcia-Mendez, E. Herbert, N. J. Dudney, J. B. Wolfenstine, J. Sakamoto and D. J. Siegel, *Chem. Mater.*, 2016, **28**, 197–206.

17 A. Sakuda, A. Hayashi, Y. Takigawa, K. Higashi and M. Tatsumisago, *J. Ceram. Soc. Jpn.*, 2013, **121**, 946–949.

18 F. P. McGrogan, T. Swamy, S. R. Bishop, E. Eggleton, L. Porz, X. Chen, Y.-M. Chiang and K. J. Van Vliet, *Adv. Energy Mater.*, 2017, **7**, 1602011.

19 G. Bucci, T. Swamy, Y.-M. Chiang and W. C. Carter, *J. Mater. Chem. A*, 2017, **5**, 19422–19430.

20 E. G. Herbert, W. E. Tenhaeff, N. J. Dudney and G. M. Pharr, *Thin Solid Films*, 2011, **520**, 413–418.

21 Y.-H. Cho, J. Wolfenstine, E. Rangasamy, H. Kim, H. Choe and J. Sakamoto, *J. Mater. Sci.*, 2012, **47**, 5970–5977.

22 R. Raj and J. Wolfenstine, *J. Power Sources*, 2017, **343**, 119–126.

23 C. Monroe and J. Newman, *J. Electrochem. Soc.*, 2004, **151**, A880–A886.

24 C. Monroe and J. Newman, *J. Electrochem. Soc.*, 2005, **152**, A396–A404.

25 K. Harry, D. Hallinan, D. Parkinson, A. MacDowell and N. P. Balsara, *Nat. Mater.*, 2014, **13**, 69–73.

26 N. S. Schausera, K. J. Harrya, D. Y. Parkinsonc, H. Watanabed and N. P. Balsara, *J. Electrochem. Soc.*, 2015, **162**, A398–A405.

27 C.-L. Tsai, V. Roddatis, V. C. Chandran, Q. Ma, S. Uhlenbruck, M. Bram, P. Heitjans and O. Guillon, *ACS Appl. Mater. Interfaces*, 2016, **8**, 10617–10626.

28 C. Fu, V. Venturi, Z. Ahmad, A. W. Ells, V. Viswanathan and B. A. Helms, 2019, arXiv: 1901.04910.

29 W. S. LePage, Y. Chen, E. Kazyak, K.-H. Chen, A. J. Sanchez, A. Poli, E. M. Arruda, M. D. Thouless and N. P. Dasgupta, *J. Electrochem. Soc.*, 2019, **166**, A89–A97.

30 B. Wang, J. Liu, Q. Sun, R. Li, T. Sham and X. Sun, *Nanotechnology*, 2014, **25**, 504007.

31 J. Liu, M. N. Banis, X. Li, A. Lushington, M. Cai, R. Li, T. Sham and X. Sun, *J. Phys. Chem. C*, 2013, **117**, 20260–20267.

32 X. Li, J. Liu, M. N. Banis, A. Lushington, R. Li, M. Cai and X. Sun, *Energy Environ. Sci.*, 2014, **7**, 768.

33 B. Wang, J. Liu, Q. Sun, B. Xiao, R. Li, T. K. Sham and X. Sun, *Adv. Mater. Interfaces*, 2016, **3**, 1600369.

34 P. Yan, J. Zheng, J. Liu, B. Wang, X. Cheng, Y. Zhang, X. Sun, C. Wang and J. G. Zhang, *Nat. Energy*, 2018, **3**, 600–605.

35 Y. Xiao, L. J. Miara, Y. Wang and G. Ceder, *Joule*, 2019, **3**, 1252–1275.

36 T. Asano and T. Komori, *US Pat*, US9379415B2, 2016, 1–13.

37 Y. Liu, Q. Sun, Y. Zhao, B. Wang, P. Kaghazchi, K. R. Adair, R. Li, C. Zhang, J. Liu, L. Y. Kuo, Y. Hu, T. K. Sham, L. Zhang, R. Yang, S. Lu, X. Song and X. Sun, *ACS Appl. Mater. Interfaces*, 2018, **10**, 31240–31248.

38 J. H. Woo, J. E. Trevey, A. S. Cavanagh, Y. S. Choi, S. C. Kim, S. M. George, K. H. Oh and S.-H. Lee, *J. Electrochem. Soc.*, 2012, **159**, A1120–A1124.

39 S. Timoshenko, *Theory of Plates and Shells*, McGraw-Hill, London, 1940.

40 A. Castellanos-Gomez, M. Poot, G. A. Steele, H. S. J. van der Zant, N. Agraït and G. Rubio-Bollinger, *Adv. Mater.*, 2012, **24**, 772–775.

41 C. Lee, X. Wei, J. W. Kysar and J. Hone, *Science*, 2008, **321**, 385–388.

42 K. Liu, Q. Yan, M. Chen, W. Fan, Y. Sun, J. Suh, D. Fu, S. Lee, J. Zhou, S. Tongay, J. Ji, B. Neaton and J. Wu, *Nano Lett.*, 2014, **14**, 5097–5103.

43 R. Zhang, V. Koutsos, R. Cheung, R. Zhang, V. Koutsos and R. Cheung, *Appl. Phys. Lett.*, 2016, **108**, 042104.

44 T. Cui, C. Cao, P. M. Sudeep, Y. Sun, T. Filleter, S. Mukherjee, J. Tam, C. V. Singh and P. M. Ajayan, *Carbon*, 2018, **136**, 168–175.

45 M. K. Tripp, C. Stampfer, D. C. Miller, T. Helbling, C. F. Herrmann, C. Hierold, K. Gall, S. M. George and V. M. Bright, *Sens. Actuators, A*, 2006, **130–131**, 419–429.

46 S. Jen, J. A. Bertrand and S. M. George, *J. Appl. Phys.*, 2011, **109**, 084305.

47 C. Cao, S. Mukherjee, J. Liu, B. Wang, M. Amirmaleki, Z. Lu, J. Y. Howe, D. Perovic, X. Sun, C. V. Singh, Y. Sun and T. Filleter, *Nanoscale*, 2017, **9**, 11678–11684.

48 Y. Tang, K. Fu and L. Chang, in *Fracture Mechanics*, ed. L. Alves, IntechOpen, 2016.

49 X. Li, D. Diao and B. Bhushab, *Acta Mater.*, 1997, **45**, 4453–4461.

50 X. Li and B. Bhushan, *Thin Solid Films*, 1998, **315**, 214–221.

51 X. Wei, Z. Meng, L. Ruiz, W. Xia, C. Lee, J. W. Kysar, J. C. Hone, S. Keten and H. D. Espinosa, *ACS Nano*, 2016, **10**, 1820–1828.

52 J. E. Sader, J. W. M. Chon and P. Mulvaney, *Rev. Sci. Instrum.*, 1999, **70**, 3967–3969.